

See discussions, stats, and author profiles for this publication at: <https://www.researchgate.net/publication/51061906>

Comparative Molecular Dynamics Study of Vapor-Exposed Basal, Prismatic, and Pyramidal Surfaces of Ice

ARTICLE *in* THE JOURNAL OF PHYSICAL CHEMISTRY A · JUNE 2011

Impact Factor: 2.69 · DOI: 10.1021/jp111359a · Source: PubMed

CITATIONS

11

READS

24

3 AUTHORS, INCLUDING:



Steven Neshyba

University of Puget Sound

32 PUBLICATIONS 650 CITATIONS

SEE PROFILE



Martina Roeselova

Academy of Sciences of the Czech Republic

46 PUBLICATIONS 893 CITATIONS

SEE PROFILE

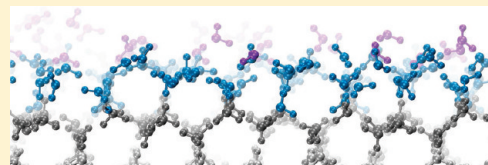
Comparative Molecular Dynamics Study of Vapor-Exposed Basal, Prismatic, and Pyramidal Surfaces of Ice

William Pfalzgraff,^{†,‡} Steven Neshyba,^{*,†} and Martina Roeselova[‡]

[†]University of Puget Sound, Tacoma, Washington 98416, United States

[‡]Institute of Organic Chemistry and Biochemistry, Academy of Sciences of the Czech Republic and Center for Biomolecules and Complex Molecular Systems, 16610 Prague 6, Czech Republic

ABSTRACT: We present the results of molecular dynamics simulations in which ice I_h slabs with free basal, prismatic, 28° pyramidal, and 14° pyramidal facets are exposed to vapor. All simulations were carried out at 250 K using a six-site intermolecular potential. Characteristics common to all facets include spontaneous development of a quasi-liquid layer (QLL) within ~ 10 ns and QLL stratification into outer (ϵ_1) and inner (ϵ_2) sublayers having on average two and three hydrogen bonds, respectively. Vapor pressure, based on the rate of escape of molecules from the QLL to the vapor phase, is found to be greatest for the 14° pyramidal and basal facets (~ 230 Pa), while significantly lower values are obtained for the prismatic and 28° pyramidal facets (~ 200 Pa). The geometric thickness of the QLL also varies between facets, with the 14° pyramidal having the greatest thickness. The free prismatic and pyramidal facets exhibit significant anisotropic diffusivity, in-plane motion being faster in the trans-prismatic direction than in the basal-to-basal direction. The in-plane diffusion length is greatest for the 28° pyramidal facet and smallest for the prismatic facet. This diversity of facet-specific properties provides a rich set of possibilities for mechanisms of ice crystal growth and ablation.



I. INTRODUCTION

Microphysical properties of cirrus clouds have long been known to influence climatologically important radiative properties of the Earth's atmosphere, primarily by reflecting visible light from the sun and by capturing infrared light from the Earth's surface.¹ Numerous radiative-transfer modeling studies have shown that the most important microphysical properties are the habit and mesoscopic (micrometer-scale) surface morphologies of ice particles.^{2–9} These properties, in turn, are a function of the history of a given cirrus cloud particle, which (at its simplest) occurs as a deposition–ablation cycle: water vapor deposits onto ice condensation nuclei in a supersaturated environment, causing growth of the ice crystals. The larger ice crystals subsequently fall into subsaturated air, where they ablate back to vapor.

The actual deposition–ablation sequence in cirrus clouds is complex enough that a great diversity of crystal habits has been observed in situ.¹⁰ For example, crystals in near-zero supersaturated cirrostratus clouds are primarily individual hexagonal plates or columns, with exterior basal (Miller–Bravais indices¹¹ (0001)) and prismatic (10 $\bar{1}$ 0) facets exposed.¹² Crystals in mid- and high-latitude cirrus clouds, in contrast, are frequently bullet rosettes with hollow ends.¹³ In very cold environments, facets identified as having Miller–Bravais indices¹¹ (10 $\bar{1}$ 1) (a 28° pyramidal facet)^{14–16} are common. The deposition–ablation cycle of cirrus clouds probably leads to a great diversity of mesoscopic morphologies as well, although this possibility is much less well documented. It has been hypothesized that mesoscopic surface roughening may account for the larger-than-expected optical backscattering characteristic of cirrus ice crystals.^{17–19}

Laboratory-grown ice crystals, for example, those grown in horizontal static diffusion chambers, exhibit a similar diversity of habits.²⁰ Recently, it has been shown that ice crystals grown on a cold stage inside a variable-pressure scanning electron microscope (VP-SEM) regularly exhibit the basal, prismatic, and 28° pyramidal facets described above, as well as the (20 $\bar{2}$ 1) facet, a 14° pyramidal facet.²¹ (Ref 21 will henceforth be referred to as PHN.) The laboratory study of PHN identified mesoscopic corrugations on prismatic facets as “trans-prismatic strands” because of their asymmetry within the prismatic plane: the corrugations exhibit a clear preference for orientation in the prismatic-to-prismatic direction.

While the phenomenology of habit morphology described above is well documented (see, e.g., ice morphology diagrams^{22–24}), it remains hard to reliably predict the habit, aspect ratio, and surface morphology of crystals that will result from a given growth environment or how existing crystals will respond to given ablation conditions. One reason for this is our limited understanding of the underlying mechanisms of growth and ablation, despite considerable progress in recent decades. In terms of vapor-deposited ice growth, an important advance was the recognition of the role of surface diffusion in controlling crystal habit via a step-growth mechanism: new ice layers are nucleated at crystal edges, followed by step growth toward the interior of the prismatic surface.²⁵

Special Issue: Victoria Buch Memorial

Received: November 30, 2010

Revised: April 4, 2011

Published: April 19, 2011

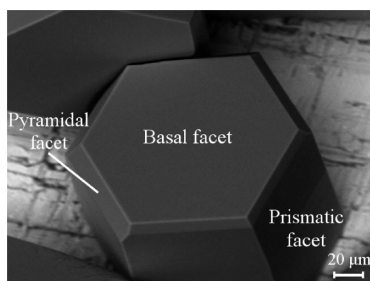


Figure 1. Scanning electron micrograph of a vapor-grown hexagonal ice crystal with the basal, prismatic, and pyramidal facets labeled. The pyramidal facet is likely the $(10\bar{1}1)$ (28°) facet.

In other theoretical frameworks, the preferential growth of certain habits is explained by structure-dependent attachment kinetics,²⁶ adjustable parametrizations of condensation coefficients,²⁷ or the combined effects of surface kinetics and gas-phase mass transport.²⁸ In terms of ice crystal sublimation, important progress has proceeded from the recognition that sublimation begins with a reverse process, i.e., formation of ablation steps at crystal edges, which then sweep inward on a crystal face.²⁹

We note that most theoretical frameworks for ice crystal growth and ablation have relied heavily on assumptions about molecular-level processes, many of which are now amenable to molecular-level experimental or theoretical investigation. Molecular-level experimental techniques have established, for example, that surface premelting of ice, described as a quasi-liquid layer (QLL, forming at temperatures above ~ 180 K³⁰), is responsible for many unique properties of ice,^{31,32} and it is now well-accepted that the QLL plays a key role in the mediation of surface diffusion as well as adsorption and desorption processes.^{31–35} Because of increases in computational and algorithmic efficiencies, molecular dynamics (MD) approaches have become increasingly useful in this connection. Classical MD simulations with empirical water–water force fields have been extensively used to obtain insight into the structure of the ice–vapor interface.^{36–41} For example, Conde et al.⁴² performed a systematic MD cross-comparison of the thickness of the QLL for the most common water models. They found that, at a given undercooling temperature (defined as $T - T_m$, where T_m is the melting point of the water model), the QLL thickness for a given crystallographic facet is largely independent of the water model. However, QLL thickness did depend on the crystallographic facet exposed, being thicker in vapor-exposed basal facets than in vapor-exposed prismatic facets. Progress in characterizing structural properties of the QLL, in turn, has led to insights into molecular-level dynamics at the ice–vapor interface. For example, the effect of surface curvature on the QLL has been investigated in a recent MD study of ice nanocolumns,⁴³ in which it was found that the ice–vapor interface formed by the secondary prismatic $(11\bar{2}0)$ facet converts spontaneously and quickly (on the order of hundreds of nanoseconds) to vapor-exposed primary prismatic $(10\bar{1}0)$ facets. MD studies have suggested that surface diffusion occurs mainly by a mechanism whereby water molecules in the QLL first migrate to the topmost sublayer of the QLL before moving horizontally over the surface and that this horizontal motion occurs with an energy of activation equal to about one hydrogen bond.^{36,44} In a recent MD study⁴⁵ of the basal ice–vapor interface, correlations were found to exist between the position of a molecule within the QLL and the likelihood that it will escape the surface.

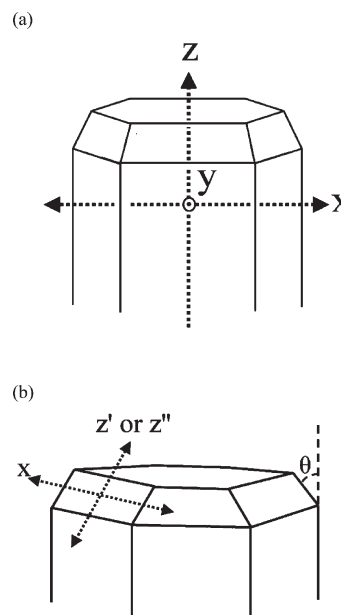


Figure 2. Coordinate systems used in MD simulations. (a) Basal and prismatic facets. (b) Pyramidal facets. The x , y' , z' and x , y'' , z'' coordinate axes were used for the $(10\bar{1}1)$ ($\theta = 28^\circ$) and $(20\bar{2}1)$ ($\theta = 14^\circ$) pyramidal facets, respectively. The y' and y'' axes (not drawn) are normal to the pyramidal surface. The x ($11\bar{2}0$) axis is common to all four coordinate systems.

The present study is motivated in general by the promise MD offers in providing molecular-level explanations for macroscopic processes such as crystal growth and ablation. In particular, we are interested in understanding the VP-SEM microscopy results of PHN, in which it is evident that different facet types respond differently to growth and ablation conditions. A VP-SEM micrograph of a laboratory-grown ice crystal that contains the major features we wish to examine is shown in Figure 1. Like the crystals shown in PHN, this crystal has exposed exterior facets designated basal (0001), prismatic ($10\bar{1}0$), and pyramidal (probably the 28° , $(10\bar{1}1)$ facet). As observed by PHN, prismatic facets typically exhibit trans-prismatic strands at near-zero supersaturation and subsaturation conditions, but the basal and pyramidal facets do not. Is there an atomistic mechanism that explains this difference?

While MD simulations have been carried out for the ice–water interface of the 14° pyramidal facet in connection with growth inhibition by antifreeze proteins,⁴⁶ its ice–vapor interface has not been previously modeled by MD, nor has the ice–vapor interface of the 28° pyramidal facet been modeled by MD, to our knowledge. As for the prismatic facet, previous MD studies have provided information regarding QLL structure, but they did not address surface dynamics or ice–vapor exchange. It is our hope that a comparative study of the ice–vapor interfaces of the basal, prismatic, 28° pyramidal, and 14° pyramidal facets will yield insights into mesoscopic structure differences observed in VP-SEM growth and ablation experiments and, more broadly, into molecular-level processes that may play a role in generating the diversity of crystal habits observed in cirrus clouds.

The paper is organized as follows. Section II presents the structure of the slab models used in our MD simulations, simulation parameters, and the intermolecular potential.

Table 1. Initial Configurations of Ice Slabs with Exposed Facets

| facet exposed | axis normal to the ice— vapor interface | thickness of unit ice layer μ_i (nm) | N^a | ice prism dimensions (nm) | L_x^b (nm) | L_y^b (nm) | L_z^b (nm) |
|----------------------|--|---|-------|--------------------------------|--------------|--------------|--------------|
| basal | z | 0.367 | 2880 | $5.39 \times 4.67 \times 3.67$ | 5.39 | 4.67 | 8.00 |
| prismatic | y | 0.389 | 2880 | $5.39 \times 4.67 \times 3.67$ | 5.39 | 8.00 | 3.67 |
| 28° pyramidal | y' | 0.343 | 2880 | $5.39 \times 4.12 \times 4.98$ | 5.39 | 9.12 | 4.98 |
| 14° pyramidal | y'' | 0.376 | 3456 | $4.04 \times 4.51 \times 6.07$ | 4.04 | 9.51 | 6.07 |

^a Number of water molecules in the simulation box. ^b Simulation box dimensions.

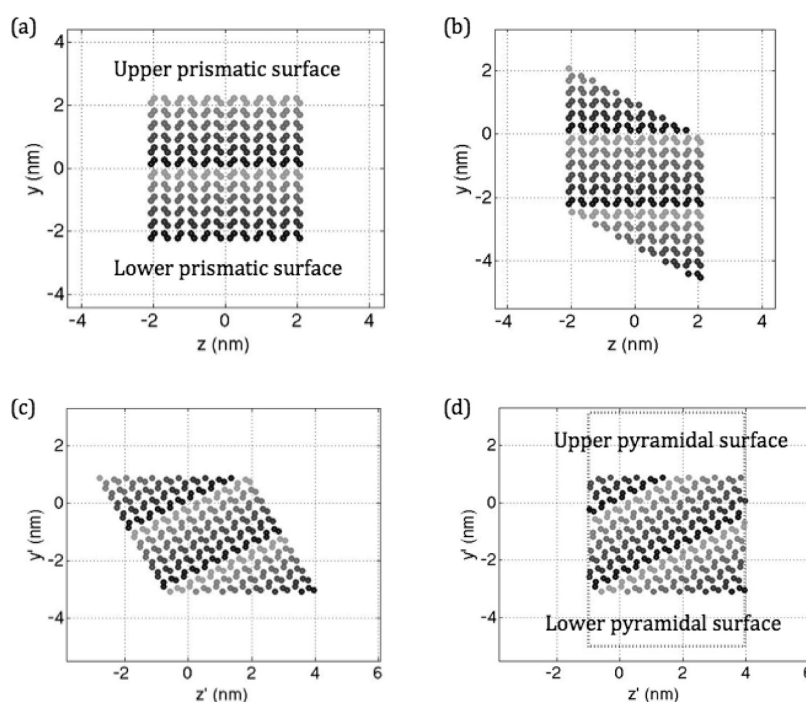


Figure 3. Construction of the 28° pyramidal ($10\bar{1}1$) slab. (a) Initial configuration. Shading indicates duplication of a 6-bilayer cube to 12 bilayers (in the y -direction). (b) Translation of selected molecules a distance $b = 4.67$ nm in the y -direction, to expose the ($10\bar{1}1$) surface. (c) Rotation about the x axis by $\theta = 28^\circ$. (d) Translation of selected molecules a distance $b/\cos(\theta) = 4.97$ nm in the z' -direction, to fit into the new simulation box. The y' -dimension of the new simulation box (shown in dashed lines) has been extended to expose the ($10\bar{1}1$) surface to vacuum. Neighbors across the periodic z' boundary (left-to-right across the vertical dashed line denoting the simulation box) are equivalent to the original neighbors across the periodic z boundary in (a) (also left-to-right).

In Section III, we present our results, including slab density profiles, vertical binding energies, vapor pressures, mass accommodation coefficients, and surface diffusivities for individual ice crystal facets. In Section IV, we discuss possible implications of our results in the framework of theories of surface dynamics and compare our results to other MD studies of ice. Section V summarizes our main conclusions.

II. METHODS

II.1. VP-SEM Microscopy. Figure 1 was generated according to methods described in PHN.²¹

II.2. Construction of Ice Slabs. Ice–vapor interfaces of the basal (0001), prismatic ($10\bar{1}0$), 28° pyramidal ($10\bar{1}1$), and 14° pyramidal ($20\bar{2}1$) facets of ice I_h were studied. The systems were constructed as ice slabs, i.e., rectangular prisms of ice in a simulation box which has been elongated a few nanometers beyond the prism size in the direction perpendicular to the desired ice–vapor interface. In constructing each slab, the initial

configuration was a rectangular ice I_h prism generated according to the proton-disordering algorithm of Buch et al.⁴⁷ This algorithm specifies orientations of water molecules such that ice I_h Bernal–Fowler constraints are satisfied for each molecule,^{48,49} including periodic neighbors across the simulation box boundaries. The axes used in our simulations are defined in Figure 2, and details of each system are given in Table 1.

The basal and prismatic slabs used in this study were initially configured as a $(N_x, N_y, N_z) = (12, 6, 10)$ prism (in the notation of Buch et al.) with dimensions $a = 5.39$, $b = 4.67$, and $c = 3.67$ nm in the x -, y -, and z -directions (see Table 1). To create the basal slab, the z -dimension of the simulation box was elongated to 8 nm. To create the prismatic slab, the y -dimension of the simulation box was elongated to 8 nm.

Construction of the ($10\bar{1}1$) pyramidal slab began with a $(N_x, N_y, N_z) = (10, 3, 12)$ prism which was duplicated in the y -direction to produce a $(N_x, N_y, N_z) = (10, 6, 12)$ prism (Figure 3a). Molecules situated above a line defined by $\theta = 28^\circ$ with respect to the prismatic plane were translated

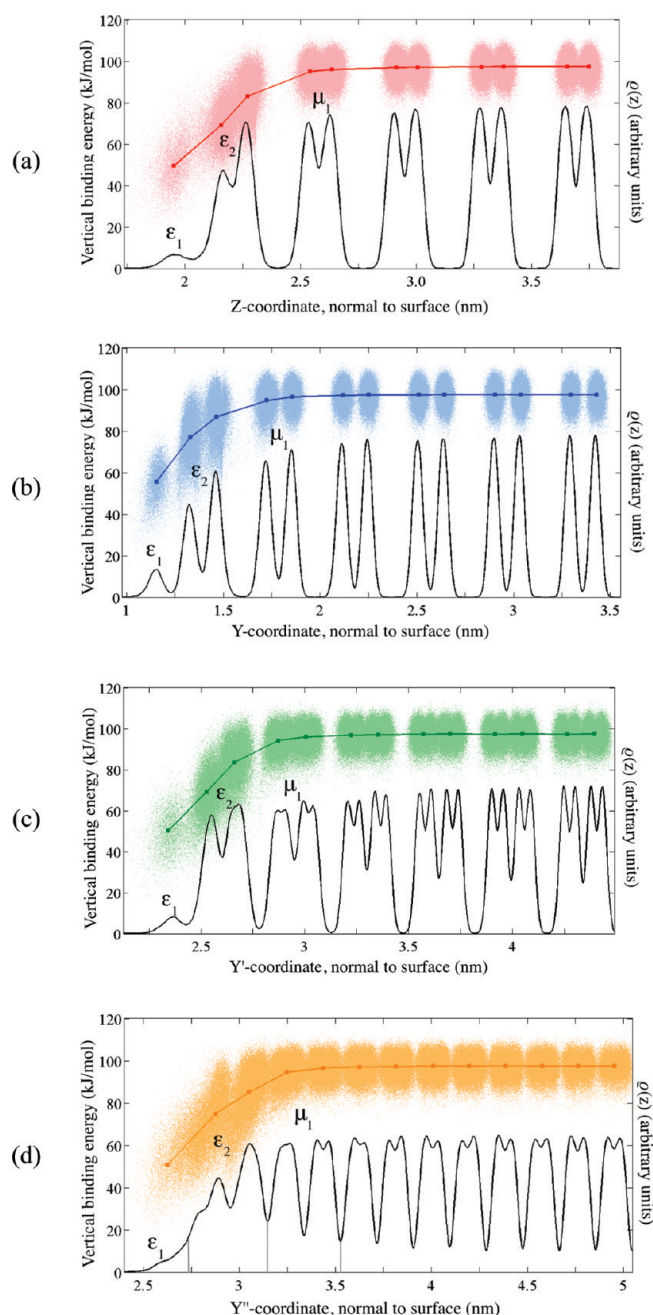


Figure 4. Density profiles of oxygen atoms (black line) and scatter plots of vertical binding energies (colored dots) of a water molecule as a function of position along the surface normal for (a) basal, (b) prismatic, (c) 28° pyramidal ($10\bar{1}1$), and (d) 14° pyramidal ($20\bar{2}1$) slabs. The left side of each plot corresponds to the ice–vapor interface and the right side to the center of the slab. Colored squares denote mean vertical binding energies in each sublayer.

downward to expose the underlying ($10\bar{1}1$) facet (Figure 3b). The new prism was then rotated so that a vector normal to the ($10\bar{1}1$) facet would coincide with the y -axis (Figure 3c); this normal is designated y' in the original coordinate system. Further translations were performed to rectangularize the system (Figure 3d). Finally, the simulation box was widened by a factor of $1/\cos(\theta)$ in the z' direction, and by an additional ~ 5 nm in the y' -direction, to create the vacuum-exposed 28° pyramidal ($10\bar{1}1$)

slab shown in Figure 3d. The foregoing manipulations were carried out to ensure that molecular configurations across the periodic z' rectangular boundary are the same as in the original ($N_x N_y N_z$) = (10, 3, 12) prism.

Construction of the ($20\bar{2}1$) pyramidal slab began with a triplicated ($N_x N_y N_z$) = (9, 2, 16) prism (hence ($N_x N_y N_z$) = (9, 6, 16)). Molecules situated above a line defined by $\theta = 14^\circ$ with respect to the prismatic plane were translated to expose the underlying ($20\bar{2}1$) facet, with subsequent manipulations analogous to those carried out for the ($10\bar{1}1$) slab (see Table 1). The axis normal to the ($20\bar{2}1$) surface is designated y'' .

To assess whether the foregoing construction of pyramidal slabs introduced any surface polarization, mean surface-normal components of dipole moment vectors of exposed bilayers were computed, for several realizations of each slab. The median absolute value of this component was ~ 0.001 D for the 28° pyramidal facet and ~ 0.01 D for the 14° pyramidal facet. For comparison, the dipole moment of the NE6 water molecule is 1.9 D.

II.3. Simulation Details. Water molecules were treated as rigid rotors interacting classically via the NE6 intermolecular potential.⁵⁰ The ice slabs were first annealed from 0 to 250 K over 5 ps and subsequently equilibrated over several nanoseconds at the target temperature. Then, the systems were allowed to evolve at 250 K ($\sim 40^\circ\text{C}$ below the NE6 melting temperature⁵¹) using Gromacs 4.0.7 and 4.5.1 molecular dynamics software⁵² in the single precision floating point mode. Production runs lasted ~ 200 ns, with configurations saved every 5 ps for further analysis. Standard 3D periodic boundary conditions were applied. Simulations were carried out under constant NVT conditions with a 1 fs integration step, and Berendsen's weak-coupling algorithm⁵³ with a time constant of 0.1 ps was used to control the temperature. A cutoff distance of 0.7 nm was used for real-space Coulombic and van der Waals interactions. The long-range Coulomb interactions were evaluated using particle-mesh Ewald summation^{54,55} with a relative tolerance of 10^{-5} , fourth-order cubic interpolation, and a Fourier spacing parameter of 0.12.

III. RESULTS

Surfaces of all slabs were found to anneal within a few nanoseconds to a disordered, premelted state that did not appear to change energetically or structurally over subsequent MD-accessible time scales (hundreds of nanoseconds). Figure 4, for example, shows symmetrized density profiles of oxygen atoms for annealed slabs, averaged over tens of nanoseconds, as a function of their position along the surface normal. Profiles based on longer trajectories showed no significant deviation from those shown. These profiles allow us to define individual layers, for which we use the ϵ/μ notation of our previous work.⁴⁵ The two sublayers nearest to the interface are denoted ϵ_1 and ϵ_2 ; the layer immediately below them is denoted μ_1 ; and the remaining interior layers are denoted μ_{2-n} . Depending on the system, these layers may consist of bilayer doublets (Figure 4a,b) or quadruplets (Figure 4c,d). The demarcation among these layer and sublayer designations is defined by density minima for all categories except the ϵ_1 – ϵ_2 boundary of the 14° pyramidal facet (Figure 4d). Since there is no minimum in the density function that would clearly mark the ϵ_1 – ϵ_2 boundary of the 14° pyramidal facet, we have designated the boundary to be a point outward from the ϵ_2 – μ_1 boundary corresponding to the ideal crystalline bilayer thickness of 0.376 nm (see Table 1), which coincides approximately with an inflection point. Also shown in the figure

Table 2. Structural Properties of the Outermost Surface Layers of Annealed Ice Slabs at 250 K

| facet exposed | geometrical thickness of $\varepsilon_1 + \varepsilon_2$ (nm) | number of $\varepsilon_1 + \varepsilon_2$ water molecules, $N_{\varepsilon_1+\varepsilon_2}$ ^a | mean population of the ε_1 sublayer ^b |
|---------------|---|---|--|
| basal | 0.67 | 288 | 7.5% |
| prismatic | 0.61 | 240 | 11.8% |
| 28° pyramidal | 0.63 | 240 | 7.7% |
| 14° pyramidal | 0.84 | 288 | 13% |

^a Number of water molecules corresponding to one unit ice layer, i.e., $N_{\varepsilon_1+\varepsilon_2} = N_{\mu_1}$. The instantaneous number of $\varepsilon_1 + \varepsilon_2$ molecules fluctuates slightly because of sublimation (sublimating molecules leaving one surface and arriving at the other surface). ^b Population of the ε_1 sublayer given in percent of the total number of $\varepsilon_1 + \varepsilon_2$ water molecules.

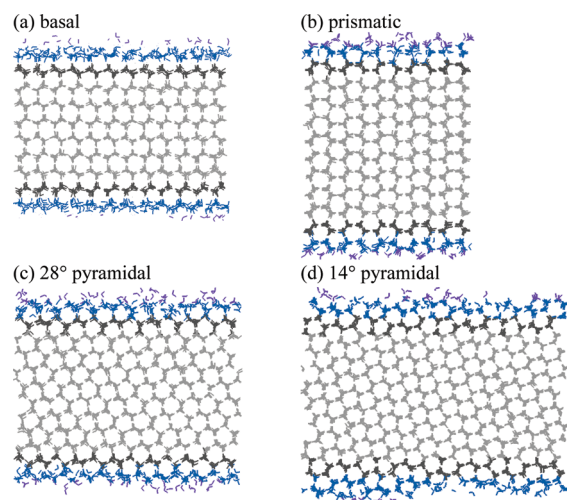


Figure 5. Snapshots of the ice slabs after tens of nanoseconds simulation time, viewed along the x (secondary prismatic) axis. Sublayers designated ε_1 and ε_2 are shown in violet and turquoise, respectively. The first crystalline-like layer (designated μ_1) is dark gray, and the inner bulk ice layers are light gray.

are scatter plots of vertical binding energies (VBEs) of water molecules, defined here as the positive difference between the total potential energy of a configuration containing the molecule and an identical configuration with the molecule removed. Figure 4 shows that a well-defined crystalline structure is present in the interior of all four ice slabs. The existence of a regular lattice inside the ice slabs is further corroborated by the vertical binding energies. All four slabs exhibit VBEs of ~ 98 kJ/mol in the inner bulk layers, which corresponds to four hydrogen bonds per water molecule, as expected for tetrahedral coordination of water in ice I_h . The average hydrogen bond strength of ~ 24.5 kJ/mol found here is consistent with the values reported for the bulk ice I_h modeled using the six-site potential⁵⁰ and differs only slightly from the experimental value of ~ 23 kJ/mol⁵⁶ for an “optimal” hydrogen bond. The degradation of the regular crystal structure near the interface is accompanied by a gradual decrease in the VBE. The mean value of VBE corresponds to ~ 80 kJ/mol in the ε_2 layer and to ~ 50 kJ/mol in the ε_1 layer for all four systems. From this we infer that on all four facets molecules in ε_1 participate in two H-bonds, while molecules in ε_2 participate in three H-bonds, on average. At the same time, there is a considerably larger spread of the VBE values in the interfacial regions compared to the interior of the slabs, indicating that a broad range of configurations with varying degree of H-bonding

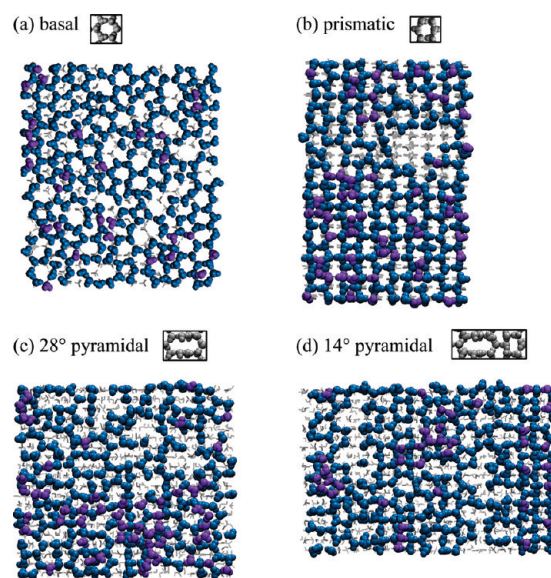


Figure 6. Plan view of slabs shown in Figure 5. Gray cut-outs show unit cells of underlying crystalline layers (μ_i).

are sampled by water molecules in the ε_1 and ε_2 sublayers of all facets.

Table 2 displays quantitative results derived from these observations. For example, the geometrical thickness of the combined $\varepsilon_1 + \varepsilon_2$ sublayers is greatest for the 14° pyramidal facet, followed by the basal, 28° pyramidal, and prismatic facets. The proportion of ε_1 molecules relative to the $\varepsilon_1 + \varepsilon_2$ population, obtained by integrating segments of the density functions appearing in Figure 4, ranges from 7.5% to 13%.

Figures 5 and 6 provide a sense of the orientations of water molecules in the ε_1 and ε_2 sublayers. Figure 5 shows side views (viewed along the secondary prismatic $(11\bar{2}0)$ axis) of vapor-exposed slabs after several tens of nanoseconds simulation time. On all four slabs, surface premelting is apparent as disordering of molecules at the ice–vapor interface. The color coding used in Figure 5 distinguishes the aforementioned layering of the ice–vapor interface. Figure 6 is a plan view of the ice slabs shown in Figure 5, with ε_1 and ε_2 molecules highlighted. Comparison of blue-colored (ε_2) molecules with the gray-colored unit cell insets shows that the ε_2 sublayer is comprised of a combination of molecules in ordered and disordered positions; there are also many gaps.

Following our previous work for the basal face,⁴⁵ we have analyzed the simulation results for layer-to-layer transitions on

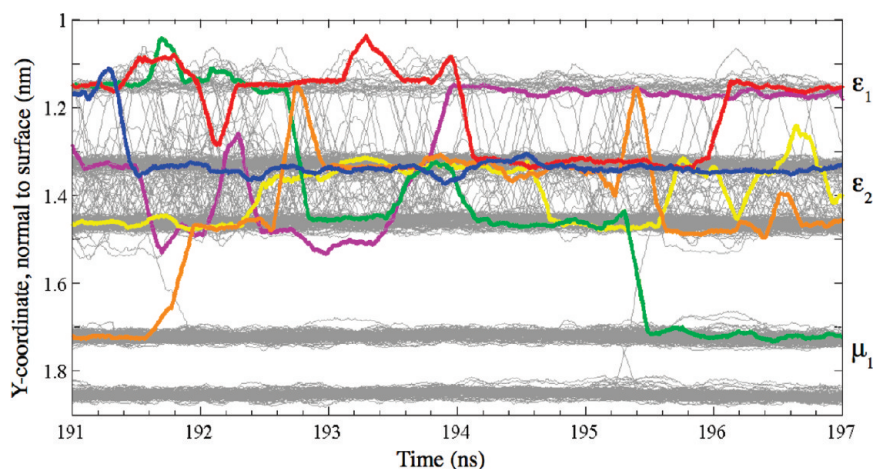


Figure 7. Trajectories along the y -coordinate (surface normal) highlighting the motion of water molecules between bilayers and within a bilayer for the prismatic slab.

different facets. The purpose of this examination is to understand the dynamics of coupling between layers and sublayers, information not contained in average density profiles such as Figure 4. As an example, Figure 7 shows the evolution of vertical (surface-normal) coordinates of oxygen atoms close to the surface of the prismatic facet, where several transitions have been highlighted. Although details of layer-to-layer dynamics vary from slab to slab, several properties of Figure 7 were observed of all four facets. First, sublimation events are rare compared to other transitions (no sublimation event occurred during the six-nanosecond range displayed in Figure 7). Second, transitions to and from layer μ_1 almost always occur as binary exchanges. This is evident in the figure as crossing trajectory lines between ϵ_2 and μ_1 at 191.8 and 195.4 ns. This behavior is consistent with an ice-like interpretation of layer μ_1 . Third, transitions between different parts of the ϵ_2 sublayer, and between ϵ_2 and ϵ_1 sublayers, are most frequent. This mobility is consistent with an interpretation of these sublayers as being partly, if not entirely, liquid-like.

We turn next to a closer investigation into mechanisms by which ϵ_2 and ϵ_1 molecules move in-plane. In-plane mobility of ϵ_1 molecules is to be expected from the energetics shown in Figure 4; since these molecules possess only two hydrogen bonds most of the time and are spatially unencumbered in at least one direction (the surface normal), they should be highly mobile. Visual inspection of trajectory animations typically reveals in-plane motion of ϵ_1 molecules after just a few tens of picoseconds. The possible participation of ϵ_2 molecules in in-plane diffusion is a different matter, however. Figure 7 shows that *some* ϵ_2 molecules move to ϵ_1 and thereby acquire in-plane mobility, but do *all* ϵ_2 molecules participate? An alternative hypothesis is that only a subset of molecules belonging to sublayer ϵ_2 are sufficiently liquid-like at the simulated temperature to transition to ϵ_1 , the remainder being ice-like and immobile. To investigate this question, we calculated the number of molecules initially belonging to sublayer ϵ_2 that have not moved out of ϵ_2 over time (Figure 8) (the figure is a composite of 50 such calculations, with their starting times separated by 0.5 ns). Near-linearity of the decay curves in a log space defines first-order e -folding times, which we will refer to hereinafter as $\epsilon_1 + \epsilon_2$ mixing times (see Table 3). These e -folding times are short compared to $\epsilon_2 \leftrightarrow \mu_1$ exchange times and sublimation times: the longest mixing time is 23 ns. Figure 9 shows a side view of a

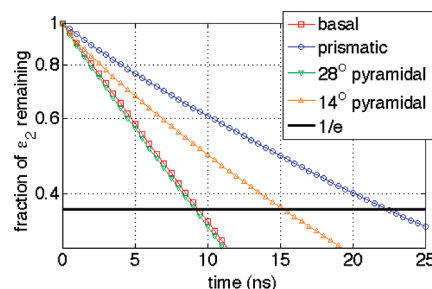
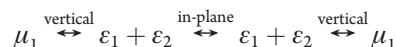


Figure 8. Fraction of molecules initially in the ϵ_2 sublayer remaining in the ϵ_2 sublayer over time. Intersections with the horizontal line coincide with e -folding lifetimes for each slab. Each curve is constructed by averaging 100 trajectories, each with starting time offset by $t_0 = 0, 0.5, 1.0, \dots$ ns.

prismatic slab after 100 ns, in which the vertical positions of molecules that have crossed in-plane periodic boundaries suggest a mechanism



as described in ref 36. A corollary of the foregoing is that the combined $\epsilon_1 + \epsilon_2$ geometric thicknesses displayed in Table 2 can be considered QLL geometric thicknesses for processes that take place on a time scale in excess of the corresponding $\epsilon_1 + \epsilon_2$ mixing times shown in Table 3.

Differences in thermodynamic stability between facets were explored in our simulations using equilibrium vapor pressure as a proxy for chemical potential. Sublimation events that occur during a simulation allow us to estimate the vapor pressure using a modified Hertz–Knudsen formula^{45,57}

$$P_{\text{vap}} = \frac{1}{2} R \sqrt{2k_B T m} \quad (1)$$

where $T = 250$ K; k_B is Boltzmann's constant; m is the mass of a water molecule; the factor of $1/2$ occurs because of the two ice–vapor interfaces in a slab; and R is the surface area-normalized sublimation rate. In our simulations, we define a sublimation event to have taken place whenever a water molecule crosses the vertical periodic boundary. Because sublimation from an ice surface at $\sim 40^\circ$ below freezing is a rather rare event on an MD

Table 3. Vertical Transition Parameters for Ice Facets at 250 K

| facet exposed | $\varepsilon_1 + \varepsilon_2$ mixing time ^a (ns) | sublimation rate, R ($\text{nm}^{-2} \text{ns}^{-1} \times 10^{-2}$) | P_{vap} (Pa) ^b | $t_e(\varepsilon_1 + \varepsilon_2 \rightarrow \text{vap})$ (ns) | $t_e(\varepsilon_1 + \varepsilon_2 \rightarrow \mu_1^c)$ (ns) | $\alpha_{\mu_1}^d$ |
|---------------|---|---|------------------------------------|--|---|--------------------|
| basal | 9 | 1.83 | 230 ± 10^e | 1200 | 700 ^f | 0.63 ^f |
| prismatic | 23 | 1.54 | 200 ± 10 | 1400 | 200 | 0.87 |
| 28° pyramidal | 9 | 1.57 | 200 ± 10 | 1700 | 50 | 0.97 |
| 14° pyramidal | 15 | 1.79 | 230 ± 10 | 1300 | 24 | 0.98 |

^a Derived from Figure 8. ^b Based on 200 ns simulation time. ^c Counting only transitions that last more than 0.5 ns. ^d Accommodation coefficient to layer μ_1 , eq 3. ^e c.f. ref 45, in which $P_{\text{vap}} = 240 \pm 50$ Pa is quoted (based on 173 ns simulation time). ^f From ref 45.

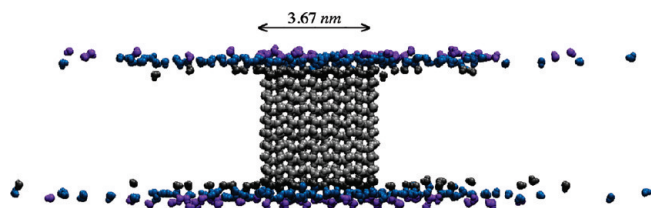


Figure 9. Prismatic surface after 100 ns, viewed along the x (secondary prismatic) axis, in which molecules crossing periodic boundaries are depicted in neighboring domains.

time scale (on average, 2–4 sublimation events per 10 ns occur for our system sizes), relatively long trajectories (>100 ns) are required to obtain converged results. The procedure for calculating R (and therefore P_{vap}) followed here differed from the procedure followed in ref 45. Rather than dividing the number of sublimation events by the total time interval (the method used in ref 45), we calculated instead the time-dependent cumulative number of sublimation events per surface area, $N_S(t)$. Linear regression of $N_S(t)$ by least-squares then yields the slope of $N_S(t)$, which is interpreted as the sublimation rate, R . This procedure is more robust in the sense that outliers at the beginning and end of a trajectory are less likely to unduly influence results. It has the additional advantage that the uncertainty in P_{vap} is calculable from the standard deviation of the best-fit slope parameter. Results for the four exposed facets are shown in Figure 10 and summarized in Table 3. The standard deviation in the slope of $N_S(t)$ was found to be <5% for all four slabs. We conclude, therefore, that values of P_{vap} for the 14° pyramidal and basal facets are significantly greater than for the prismatic and 28° pyramidal facets. Note that the uncertainty in the value obtained here for the basal facet (± 10 Pa) is smaller than the uncertainty quoted in ref 45 (± 50 Pa) because of the longer trajectory and more robust analysis employed here.

The foregoing shows that transitions from the surface to the vapor phase and accommodation to the bulk are both slow compared to $\varepsilon_1 + \varepsilon_2$ mixing. Assuming first-order kinetics, this difference permits calculation of e -folding lifetimes for vaporization ($\varepsilon_1 + \varepsilon_2 \rightarrow \text{vapor}$) and for accommodation to the bulk ($\varepsilon_1 + \varepsilon_2 \rightarrow \mu_1$), according to⁴⁵

$$t_e(\varepsilon_1 + \varepsilon_2 \rightarrow \text{vapor}) = \frac{N_{\varepsilon_1 + \varepsilon_2}}{f_{\varepsilon_1 + \varepsilon_2 \rightarrow \text{vapor}}} \quad (2a)$$

$$t_e(\varepsilon_1 + \varepsilon_2 \rightarrow \mu_1) = \frac{N_{\varepsilon_1 + \varepsilon_2}}{f_{\varepsilon_1 + \varepsilon_2 \rightarrow \mu_1}} \quad (2b)$$

where $N_{\varepsilon_1 + \varepsilon_2}$ is the number of water molecules in the $\varepsilon_1 + \varepsilon_2$ layer and the denominator is understood to be the rate of

transitions out of the $\varepsilon_1 + \varepsilon_2$ layer per unit time. (Note that $f_{\varepsilon_1 + \varepsilon_2 \rightarrow \text{vapor}}$ is related to the aforementioned sublimation rate, R , except that it is not normalized to unit surface area.) From these lifetimes, we obtain an accommodation coefficient for incorporation into the bulk μ_1 layer according to⁴⁵

$$\alpha_{\mu_1} = \alpha_s \frac{t_e^{-1}(\varepsilon_1 + \varepsilon_2 \rightarrow \mu_1)}{t_e^{-1}(\varepsilon_1 + \varepsilon_2 \rightarrow \mu_1) + t_e^{-1}(\varepsilon_1 + \varepsilon_2 \rightarrow \text{vapor})} \quad (3)$$

where α_s is the sticking (surface accommodation) coefficient, defined as the number of water vapor molecules that adsorb onto the ice surface divided by the number of water vapor molecules striking the surface. On the basis of our previous work,⁴⁵ we assume here that $\alpha_s \approx 1$. The e -folding lifetimes as well as the accommodation coefficients for the μ_1 layer are given in Table 3. The vaporization lifetimes are shortest for the basal facet and the 14° pyramidal facet, followed by the prismatic facet and the 28° pyramidal facet, consistent with an inverse trend in vapor pressure. The lifetimes with respect to the transitions between $\varepsilon_1 + \varepsilon_2$ and the first bulk ice layer, μ_1 , decrease significantly in the order basal > prismatic > 28° pyramidal > 14° pyramidal. This trend is reflected in values of α_{μ_1} , which increase in the order basal < prismatic < 28° pyramidal < 14° pyramidal. We note that computed values of the “bulk” accommodation coefficient depend strongly on the choice of μ_1 as the relevant bulk layer. Since we observed no transitions to or from deeper ice layers during the course of our simulations, choosing $\mu_{i>1}$ instead of μ_1 would result in a value of the accommodation coefficient approaching zero.

Mesoscopic structures noted by PHN on the prismatic facets of ice crystals exhibit a strong directional anisotropy. To investigate whether this preference could be related to surface diffusion, we calculated one-dimensional mean-square displacements (MSD) of water oxygen atoms. Mean one-dimensional MSD functions were averaged over different starting times, spaced at intervals of 0.2 ns. In a typical case, a trajectory of 90 ns, after omitting the first 10 ns for annealing, allowed us to average 225 mean one-dimensional MSD functions of 50 ns. Sublimating molecules were excluded from these calculations, but since these were relatively few, the resulting MSD functions are not likely to be influenced significantly. Figure 11 shows averaged MSD functions for all four facets. From the figure, it is evident that diffusion on the prismatic and both pyramidal facets is anisotropic. On all three facets, diffusion in the trans-prismatic (x) direction is faster than in the basal-to-basal (z, z' , or z'') direction. (As a check, we have performed some preliminary runs in double precision for the basal and prismatic facets. These results suggest that while the resulting diffusivity coefficients are slightly different from those shown in Figure 11 the anisotropies remain.) In contrast, the basal facet exhibits no significant anisotropy.

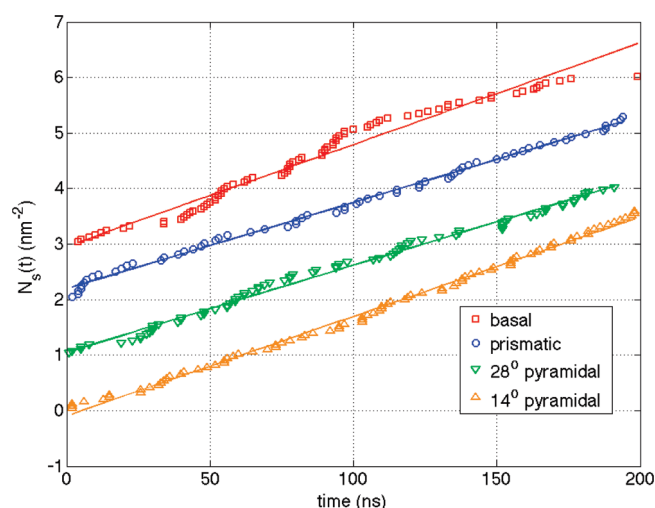


Figure 10. Cumulative surface-to-vapor departure functions, $N_s(t)$. Curves are offset to show best fit lines for each facet.

Regarding the quantitative measurement of surface diffusivity, we note that in general a one-dimensional diffusion coefficient, D , can be obtained from the slope of a plot of a one-dimensional MSD (as in Figure 11) of all molecules in the slab as a function of time using the one-dimensional Einstein relation⁵⁸

$$D = \frac{1}{2} \frac{d\text{MSD}}{dt} \quad (4)$$

Since molecules in bulk ice do not contribute to the MSD, we define a surface diffusion coefficient, D^* , according to

$$D^* = D/Q \quad (5)$$

where Q is the ratio of the number of nonbulk molecules to the total number of molecules in the slab. If we identify nonbulk molecules as the combined $\varepsilon_1 + \varepsilon_2$ sublayers, we have

$$Q = \frac{N_{\varepsilon_1 + \varepsilon_2}}{N_{\text{slab}}} \quad (6)$$

Values of D^* obtained in this way, shown in Table 4, suggest the fastest diffusion on the basal surface and slowest diffusion on the prismatic surface, but it should be noted that such comparisons depend on the value of Q assigned to the slab; effectively this means that assumptions about the thickness of the QLL limit our ability to compare diffusivity of one facet to another. To circumvent this restriction, it is desirable to construct a diffusivity-related quantity that does *not* depend on any particular designation of surface molecules. One such quantity is the diffusion length, given by⁵⁹

$$x_s = \sqrt{D^* t_e} \quad (7)$$

where t_e is a surface \rightarrow vapor lifetime. Physically, x_s indicates the mean distance an adsorbed molecule will migrate on a surface before it desorbs. The independence of x_s with respect to the designation of QLL molecules is shown by combining eq 2a with eqs 4–7, yielding

$$x_s = \sqrt{\frac{N_{\text{slab}}}{2f_{\varepsilon_1 + \varepsilon_2 \rightarrow \text{vapor}}} \frac{d\text{MSD}}{dt}} \quad (8)$$

Properly speaking, the frequency term in the denominator should include the effects of vaporization from parts of the

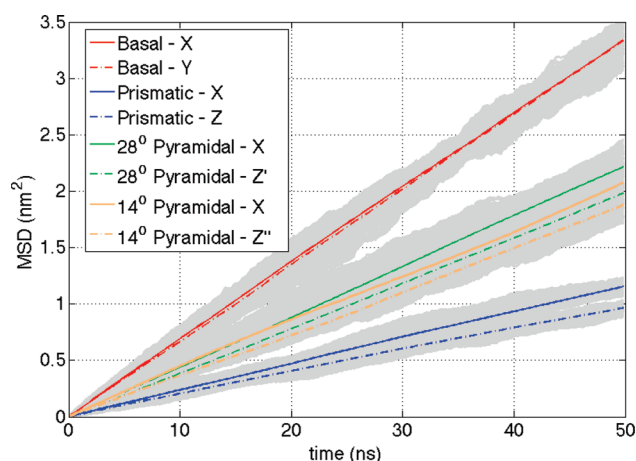


Figure 11. One-dimensional in-plane mean square displacement of oxygen atoms, as a function of time. Gray shading shows the range of values spanned by individual trajectory segments.

Table 4. MD-Derived One-Dimensional Diffusivity Parameters of Ice Facets

| facet exposed | direction of diffusion | Q | one-dimensional diffusivity, D^* ($\text{cm}^2/\text{s} \times 10^{-6}$) | diffusion length, x_s (nm) |
|---------------|------------------------|-----|--|------------------------------|
| basal | x | 1/5 | 1.67 | 14.2 |
| | y | 1/5 | 1.68 | 14.2 |
| prismatic | x | 1/6 | 0.70 | 9.9 |
| | z | 1/6 | 0.58 | 9.0 |
| 28° pyramidal | x | 1/6 | 1.34 | 15.1 |
| | z' | 1/6 | 1.20 | 14.3 |
| 14° pyramidal | x | 1/6 | 1.21 | 12.5 |
| | z'' | 1/6 | 1.13 | 12.1 |

surface other than ε_1 or ε_2 , but this is a negligible effect at the temperature considered here.⁴⁵ Values of x_s are given in Table 4. The shortest diffusion length occurs on the prismatic surface in the basal-to-basal (z) direction, coinciding with the smallest diffusion coefficient, D^* . One might expect the longest diffusion length to occur on the surface with the highest diffusivity, i.e., the basal surface, but the high sublimation rate of the basal surface has the compensating effect of shortening the diffusion length. Instead, the longest diffusion length occurs on the 28° pyramidal surface, in the trans-prismatic (x) direction.

IV. DISCUSSION

Regarding the number of ice layers constituting the QLL, previous MD simulations of basal and prismatic ice–vapor interfaces at undercooling temperatures similar to that employed here ($T - T_m \approx -40$ °C) exhibited a QLL which consists of water molecules from the single ice bilayer closest to the ice–vapor interface, irrespective of the water model used.^{41,42,44} Our results support this picture for basal and prismatic surfaces and extend it to the two pyramidal facets for which the free ice–vapor interface had not been previously modeled using MD.

It has been argued elsewhere⁴² that at a given temperature the basal QLL is geometrically thicker than the prismatic QLL. Our

results are consistent with this ranking. The 14° pyramidal QLL thickness, which has not been previously documented, appears to be even thicker than the basal QLL.

Numerous theoretical and experimental studies of diffusion dynamics on the surface of ice point to a mechanism in which molecules in lower bilayers move to the surface before translating, i.e., a vacancy-mediated model.^{36,60,61} In one study, Arrhenius analysis of surface diffusion in MD-simulated TIP4P ice indicated an activation energy equivalent to about one hydrogen bond, suggesting a mechanism by which molecules move by repeatedly breaking and forming hydrogen bonds.³⁶ Our estimates of surface diffusion coefficients are within the same order of magnitude as these results, although (as described in Section III) our values depend on the validity of an assumption that the QLL consists of only molecules in sublayers $\varepsilon_1 + \varepsilon_2$.

Anisotropic diffusivity has long been recognized on facets of other crystalline substances, for example, of admolecules on TiO_2 -(110)^{62,63} and self-diffusion on $\text{Pt}(110)$.⁶⁴ In the latter case, anisotropic surface free energy was invoked to explain the anisotropic diffusivity. If similar mechanisms are at work in the present context, the pertinent question may be why the basal slab does *not* exhibit anisotropic diffusivity. It may be that the 6-fold (in-plane) symmetry of the basal facet renders the difference between any two right angles too small to be detected within the limited trajectory times of MD undertaken here. A temperature-dependent study of diffusivity may shed more light on reasons for these properties.

In the theoretical framework of Chen and Lamb,²⁸ the effects of surface kinetics and gas-phase mass transport from one facet to another are invoked to account for the habits of ice crystals grown by vapor deposition. Both effects are somewhat problematic from an empirical point of view, in the sense that neither is easily accessible to measurement. The surface kinetic effect, for example, is described as the difference in condensation coefficients between basal and prismatic facets, but the condensation coefficient itself depends on the local excess density of vapor, which can vary over a given facet. The present results contribute to this picture in a small way, in that the concept of “local excess density of vapor” depends fundamentally on the intrinsic sublimation rate of a given facet. Our finding that sublimation rates (presented here as equivalent vapor pressures) are facet-specific, with higher values associated with the basal and 14° pyramidal facets compared to prismatic and 28° pyramidal facets at 250 K, provides an atomistic grounding to this view.

As mentioned in Section I, prevailing models of ice crystal growth specify that new ice layers be nucleated at crystal edges, followed by step growth toward the interior of a facet. Step growth models can be characterized as stable, in which steps proceed as smooth fronts, or unstable, in which small perturbations in a step front are amplified (“Bales–Zangwill instability”^{59,65}). The Bales–Zangwill model predicts that stable step growth is favored by short surface diffusion lengths (x_s). As Table 4 shows, the prismatic surface exhibits exceptionally low values of the surface diffusion length compared to other facets and significant diffusive anisotropy. A speculative narrative of prismatic-surface crystal growth could be constructed as follows: in high supersaturation conditions, nucleation at a prismatic–prismatic edge leads to step growth which is stable (because x_s is small) and which proceeds preferentially in trans-prismatic direction (because of diffusive anisotropy). Lower supersaturation conditions cause, by an unknown mechanism, larger surface diffusion lengths, hence a transition to unstable step growth. Unstable step growth is eventually manifested as the mesoscopic

structures observed by PHN.²² Such speculations must be considered quite tentative, however, in the absence of a firmer atomistic framework for ice crystal growth; in particular, we note that MD simulation of nucleation of new ice layers at crystal edges has not yet been presented.

V. CONCLUSIONS

We present the results of molecular dynamics simulations in which ice I_h slabs with free basal, prismatic, 28° pyramidal, and 14° pyramidal facets are exposed to vapor. Our goal is to gain insight into atomistic processes relevant to growth and ablation of vapor-deposited ice crystals. All simulations are carried out using the NE6 water model at a nominal temperature of 250 K, which is $\sim 40^\circ\text{C}$ below the model melting temperature. Bases of comparison include density profiles, vertical binding energies, vapor pressures, and surface diffusivities of molecules, all processes primarily associated with the quasi-liquid layer (QLL) of the ice slabs at this temperature.

The four facets exhibit several features in common. When perfect crystalline surfaces are first exposed to vacuum, all facets develop a fully annealed (i.e., statistically unchanging) QLL within 10 ns. Vertical binding energies of molecules in the QLL range from values corresponding to three hydrogen bonds (the “ ε_2 ” sublayer) to values corresponding to two hydrogen bonds (“ ε_1 ”). Mixing between sublayers ε_2 and ε_1 occurs on a time scale shorter than 25 ns for all four facets.

We find that some facets stand out in certain respects. For example, the 14° pyramidal facet stands out as having a poorly defined separation between ε_2 and ε_1 sublayers: the transition of vertical binding energies from three to two hydrogen bonds along the surface normal is smooth and is marked structurally only by an inflection (rather than a minimum) in the density profile. By contrast, the density profiles of the other three facets each exhibit a point at which a distinct minimum between ε_1 and ε_2 appears; this separation point also separates clusters of vertical binding energies corresponding to those sublayers.

The basal facet stands out as being the only facet that does *not* exhibit anisotropic surface diffusivity. By contrast, the prismatic and both pyramidal facets exhibit distinctly anisotropic surface diffusivity, diffusion being faster in the trans-prismatic direction than in the basal-to-basal direction for all three facets. We speculate that the basal facet’s 6-fold in-plane symmetry is responsible for the absence of diffusive anisotropy in that slab.

A third division concerns the surface diffusion length, which is interpreted as the distance an adsorbed molecule is likely to travel before desorbing. The surface diffusion length is useful for quantitative comparisons between facets because it does not depend on variations in QLL thickness from facet to facet. Here, the stand-out is the prismatic facet: water vapor molecules landing on the prismatic facet surface travel only 9 nm in the basal-to-basal (z) direction before desorbing, compared to distances in the 12–15 nm range for other facets.

The diversity of facet-specific properties documented here suggests a wide range of possibilities for hosting admolecules that, in combination with their temperature dependences, would appear to provide useful constraints in understanding ice crystal growth.

■ ACKNOWLEDGMENT

We thank Jan Heyda, Ondrej Marsalek, Pavel Jungwirth, Billy Wonderly, and Penny Rowe for fruitful discussions. We also

thank two anonymous reviewers for their care and insight in reviewing the manuscript. This work has been supported by the Czech Science Foundation (grant P208/10/1724), the Ministry of Education of the Czech Republic (grants ME09064 and LC512), the Academy of Sciences of the Czech Republic (project AV0Z40550506), and the University of Puget Sound. The authors would also like to acknowledge a particular debt to Viki Buch in connection with this work. Nearly a decade ago, during a visit to the University of Puget Sound, one of the authors (SPN) showed her a set of SEM images of ice. The variation in the ice habits was striking—hollowing, bullet rosettes, clustering, and other strange habits. When Viki posed the question, “why do those crystals grow that way?” it was clear that she meant it in the sense that, if we were smart enough, we could understand it in a fundamental, physical chemistry way—at a molecular level. That comment, eventually, led to the present work.

REFERENCES

- (1) Stephens, G. L.; Tsay, S. C.; Stackhouse, P. W., Jr.; Flatau, P. J. *J. Atmos. Sci.* **1990**, *47*, 1742–1754.
- (2) Takano, Y.; Liou, K. N. *J. Atmos. Sci.* **1995**, *52*, 818–837.
- (3) Kinne, S.; Liou, K. N. *Atmos. Res.* **1989**, *24*, 273–284.
- (4) Neshyba, S. P.; Grenfell, T. C.; Warren, S. G. *J. Geophys. Res.* **2003**, *108*, 4448.
- (5) Grenfell, T. C.; Neshyba, S. P.; Warren, S. G. *J. Geophys. Res.* **2005**, *110*, D17203.
- (6) Gierens, K. M.; Monier, M.; Gayet, J. F. *J. Geophys. Res.* **2003**, *108*, 4069.
- (7) Karcher, B.; Lohmann, U. *J. Geophys. Res.* **2002**, *107*, 4698.
- (8) Korolev, A. V.; Isaac, G. A.; Hallett, J. *Geophys. Res. Lett.* **1999**, *26*, 1299–1302.
- (9) Fu, Q.; Liou, K. N. *J. Atmos. Sci.* **2008**, *50*, 13.
- (10) Monier, M.; Wobrock, W.; Gayet, J. F.; Flossmann, A. *J. Atmos. Sci.* **2006**, *63*, 504–525.
- (11) Pruppacher, H.; Klett, J. *Microphysics of Clouds and Precipitation*, 1st ed.; Springer: Berlin, 1996.
- (12) Weickmann, H. *The Ice Phase in the Atmosphere*; Royal Aircraft Establishment: London, 1948.
- (13) Schmitt, C. G.; Heymsfield, A. J. *J. Atmos. Sci.* **2007**, *64*, 4514–4519.
- (14) Goldie, E.; Meaden, G.; White, R. *Weather* **1976**, *31*, 304–311.
- (15) Greenler, R. *Rainbows, Halos and Glories*, 1st ed.; Cambridge University Press: New York, 1980.
- (16) Neiman, P. J. *B. Am. Meteorol. Soc.* **1989**, *70*, 258–264.
- (17) Garrett, T. Observational quantification of the optical properties of cirrus cloud. In *Light Scattering Reviews: Light Scattering and Reflection*; Kokhanovsky, A., Ed.; Praxis: Chichester, U.K., 2008; Vol. 3, p 3.
- (18) Ulanowski, Z.; Hesse, E.; Kaye, P. H.; Baran, A. J. *J. Quant. Spectrosc. Radiat. Transfer* **2006**, *100*, 382–392.
- (19) Yang, P.; Liou, K. N. *Contrib. Atmos. Phys.* **1998**, *71*, 223–248.
- (20) Bailey, M.; Hallett, J. *J. Atmos. Sci.* **2004**, *61*, 514–544.
- (21) Pfalzgraff, W. C.; Hulscher, R. M.; Neshyba, S. P. *Atmos. Chem. Phys.* **2010**, *10*, 20739–20763.
- (22) Magono, C.; Lee, C. *J. Fac. Sci. Hokkaido Univ.* **1966**, *2*, 320–335.
- (23) Kobayashi, T. *Philos. Mag.* **1961**, *6*, 1363–1370.
- (24) Bailey, M. P.; Hallett, J. *J. Atmos. Sci.* **2009**, *66*, 2888.
- (25) Hobbs, P.; Scott, W. *J. Geophys. Res.* **1965**, *70*, 5025–5034.
- (26) Libbrecht, K. G. *J. Cryst. Growth* **2003**, *258*, 168–175.
- (27) Nelson, J. T.; Baker, M. B. *J. Geophys. Res.* **1996**, *7033*–7047.
- (28) Chen, J.; Lamb, D. *J. Atmos. Sci.* **1994**, *51*, 1206–1222.
- (29) Nelson, J. *J. Atmos. Sci.* **1998**, *55*, 910–919.
- (30) Suter, M. T.; Andersson, P. U.; Pettersson, J. B. C. *J. Chem. Phys.* **2006**, *125*, 174704.
- (31) Li, Y.; Somorjai, G. A. *J. Phys. Chem. C* **2007**, *111*, 9631–9637.
- (32) Sazaki, G.; Zepeda, S.; Nakatsubo, S.; Yokoyama, E.; Furukawa, Y. *Proc. Natl. Acad. Sci. U.S.A.* **2010**, *107*, 19702.
- (33) Batista, E. R.; Ayotte, P.; Bilic, A.; Kay, B. D.; Jonsson, H. *Phys. Rev. Lett.* **2005**, *95*, 223201–223204.
- (34) Sadtchenko, V.; Brindza, M.; Chonde, M.; Palmore, B.; Eom, R. *J. Chem. Phys.* **2004**, *121*, 11980.
- (35) Lu, H.; McCartney, S. A.; Chonde, M.; Smyla, D.; Sadtchenko, V. *J. Chem. Phys.* **2006**, *125*, 44709–44711.
- (36) Bolton, K.; Pettersson, J. B. *J. Phys. Chem. B* **2000**, *104*, 1590–1595.
- (37) Kroes, G. J.; Clary, D. C. *J. Phys. Chem.* **1992**, *96*, 7079–7088.
- (38) Kroes, G. J. *Surf. Sci.* **1992**, *275*, 365–382.
- (39) Ikeda-Fukazawa, T.; Kawamura, K. *J. Chem. Phys.* **2004**, *120*, 1395.
- (40) Vega, C.; Martin-Conde, M.; Patrykiewicz, A. *Mol. Phys.* **2006**, *104*, 3583–3592.
- (41) Bishop, C. L.; Pan, D.; Liu, L. M.; Tribello, G. A.; Michaelides, A.; Wang, E. G.; Slater, B. *Faraday Discuss* **2009**, *141*, 277–292.
- (42) Conde, M. M.; Vega, C.; Patrykiewicz, A. *J. Chem. Phys.* **2008**, *129*, 14702.
- (43) Pereyra, R. G.; Carignano, M. A. *J. Phys. Chem. C* **2009**, *113*, 12699–12705.
- (44) Picaud, S. *J. Chem. Phys.* **2006**, *125*, 174712.
- (45) Neshyba, S. P.; Nugent, E.; Roeselová, M.; Jungwirth, P. *J. Phys. Chem. C* **2009**, *113*, 4597–4604.
- (46) Nada, H.; Furukawa, Y. Growth Kinetics on Interface Between 2021 Plane of Ice and Water Investigated by a Molecular Dynamics Simulation. In *Physics and Chemistry of Ice*; Kuhs, W. F., Ed.; Royal Society of Chemistry: Cambridge, U.K., 2007.
- (47) Buch, V.; Sandler, P.; Sadlej, J. *J. Phys. Chem. B* **1998**, *102*, 8641–8653. It should be noted that Dr. Buch almost certainly would have disapproved of the way we have constructed the pyramidal surfaces here and instead recommended reformulation of the algorithm in the rotated coordinate system.
- (48) Bernal, J. D.; Fowler, R. H. *J. Chem. Phys.* **1933**, *1*, 515.
- (49) Pauling, L. *J. Am. Chem. Soc.* **1935**, *57*, 2680–2684.
- (50) Nada, H.; van der Eerden, J. *J. Chem. Phys.* **2003**, *118*, 7401.
- (51) Abascal, J. L. F.; Fernandez, R. G.; Vega, C.; Carignano, M. A. *J. Chem. Phys.* **2006**, *125*, 166101–166102.
- (52) Lindahl, E.; Hess, B.; van der Spoel, D. *J. Mol. Model.* **2001**, *7*, 306–317.
- (53) Berendsen, H. J. C.; Postma, J. P. M.; van Gunsteren, W. F.; DiNola, A.; Haak, J. R. *J. Chem. Phys.* **1984**, *81*, 3684.
- (54) Darden, T.; York, D.; Pedersen, L. *J. J. Chem. Phys.* **1993**, *98*, 10089–10092.
- (55) Essmann, U.; Perera, L.; Berkowitz, M. L.; *J. Chem. Phys.* **1995**, *103*, 8577.
- (56) Suresh, S. J.; Naik, V. M. *J. Chem. Phys.* **2000**, *113*, 9727.
- (57) Saito, Y. *Statistical Physics of Crystal Growth*; World Scientific: Singapore, 1996.
- (58) Allen, M.; Tildesley, D. J. *Computer Simulation of Liquids*; Oxford University Press Inc.: Oxford, 1987.
- (59) Bales, G. S.; Zangwill, A. *Phys. Rev. B* **1990**, *41*, 5500.
- (60) Livingston, F. E.; Smith, J. A.; George, S. M. *J. Phys. Chem. A* **2002**, *106*, 6309–6318.
- (61) Brown, D. E.; George, S. M. *J. Phys. Chem.* **1996**, *100*, 15460.
- (62) Onishi, H.; Iwasawa, Y. *Langmuir* **1994**, *10*, 4414–4416.
- (63) Onishi, H.; Fukui, K.; Iwasawa, Y. *Colloid Surf., A* **1996**, *109*, 335–343.
- (64) Preuss, E.; Freyer, N.; Bonzel, H. P. *Appl. Phys. A: Mater. Sci. Process.* **1986**, *41*, 137–143.
- (65) Li, B.; Lowengrub, J.; Ratz, A.; Voight, A. *Commun. Comput. Phys.* **2009**, *6*, 433–482.